Stable Pentagonal 2D Palladium Diselenide Enables Rapid Electrosynthesis of Hydrogen Peroxide

R. Dominic Ross, Kwanpyung Lee, Gerardo J. Quintana Cintrón, Kaylin Xu, Hongyuan Sheng, JR Schmidt, and Song Jin**

Department of Chemistry, University of Wisconsin–Madison, 1101 University Avenue, Madison, Wisconsin 53706, United States

*Corresponding author emails: schmidt@chem.wisc.edu; jin@chem.wisc.edu

ABSTRACT

Electrosynthesis of hydrogen peroxide (H_2O_2) via the two-electron oxygen reduction reaction ($2e^-$ ORR) is promising for various practical applications such as wastewater treatment. However, few electrocatalysts are active and selective for $2e^-$ ORR yet also resistant to catalyst leaching under realistic operating conditions. Here, a joint experimental and computational study reveals active and stable $2e^-$ ORR catalysis in neutral media over 2D layered $PdSe_2$ with a unique pentagonal puckered ring structure type. Computations predict active and selective $2e^-$ ORR on the basal plane and edge of $PdSe_2$, but with distinct kinetic behaviors. Electrochemical measurements of hydrothermally synthesized $PdSe_2$ nanoplates show higher $2e^-$ ORR activity than other Pd-Se compounds (Pd_4Se and $Pd_{17}Se_{15}$). $PdSe_2$ on a gas diffusion electrode can rapidly accumulate H_2O_2 in buffered neutral solution under high current density. The electrochemical stability of $PdSe_2$ is further confirmed by long device operational stability, elemental analysis of the catalyst and electrolyte and synchrotron X-ray absorption spectroscopy. This work establishes a new efficient and stable $2e^-$ ORR catalyst at practical current densities and opens catalyst designs utilizing the unique 2D pentagonal structure motif.

INTRODUCTION

Hydrogen peroxide (H_2O_2) is a green oxidant with diverse applications including disinfection, wastewater treatment, and chemical synthesis.[1,2] The current "anthraquinone process" for chemical production of H_2O_2 is energy intensive, highly centralized and requires hazardous transportation of concentrated H_2O_2 solutions. This hazard is unnecessary when considering that many applications use dilute H_2O_2 solutions, or low concentrations of transient H_2O_2.[3] The electrosynthesis of H_2O_2 via the two-electron oxygen reduction reaction ($2e^-$ ORR) could be a promising alternative, especially for applications requiring on-demand or continuous production of low concentrations of H_2O_2, if catalysts with high activity, selectivity and stability for $2e^-$ ORR (versus the four electron oxygen reduction reaction to water, $4e^-$ ORR) can be identified. Even though there are many recent reports on carbon-based and metal compound catalysts that are active in alkaline (or acidic) media,[4–12] reports of catalysts selective for $2e^-$ ORR in neutral media, in which H_2O_2 could be stored and directly utilized without post-treatment, have been more limited,[13–17] especially in buffered neutral media where the activity is not a result of a shift towards alkaline pH during operation.[7] Metal compounds are particularly interesting for this catalytic challenge on account of their natural active site separation, which can serve as a kinetic barrier to the $4e^-$ ORR, and their tunable structures that can enable systematic characterization of the structure-property relationships.[7]

A crucial consideration for the practical electrosynthesis of H_2O_2 is the stability of these emerging metal-containing electrocatalysts. Electrocatalysts for $2e^-$ ORR must be (i) stable against leaching of metals and other non-metal elements (ORR inert sites), (ii) prevent activity degradation and (iii) decomposition of the electrosynthesized H_2O_2.[4] Preventing leaching is especially important for wastewater treatment to ensure the catalyst does not lead to further contamination.

The Environmental Protection Agency (EPA) limits Se in drinking water to 0.05 ppm as well as limits (or requires concentration monitoring of) metals such as Co and Cu. Metal leaching can also lead to degradation of catalytic activity during continuous operation and accelerate the reduction of accumulated H_2O_2.[18,19] Compounds containing noble metals (such as Au, Rh, and Pd) promise better stability based on their bulk Pourbaix diagrams and DFT calculations predicted some to have high activity towards $2e^-$ ORR.[20] The higher cost of noble metals compared to earth-abundant metals could be necessary for applications where greater stability is crucial, particularly on-site applications where the produced H_2O_2 will be used directly without further purification. Specifically, recent experimental studies on amorphous Pd,[21,22] amorphous Pd-Se nanoparticles,[23] and Pd_4Se nanoparticles for $2e^-$ ORR,[24] as well as the theoretical prediction that some Pd-Se compounds are stable and active for $2e^-$ ORR suggest that the separation of Pd atoms by Se atoms likely leads to both high selectivity for $2e^-$ ORR[7] and good stability due to selenium's improved resistance to oxidation (relative to sulfides).[25]

Among the 10+ possible Pd-Se compounds and polymorphs,[26,27] the most stable orthorhombic polymorph of $PdSe_2$ has a unique two-dimensional (2D) pentagonal structure where Se_2^{2-} dumbbells form five-membered rings with Pd in puckered layers (Figure 1a). 2D $PdSe_2$ has been increasingly exploited for optoelectronic device applications due to its interesting electronic properties,[28,29] layer-number tunable bandgap,[30–32] and optical nonlinearity.[33] Several characteristics of this unique layered $PdSe_2$ structure type also make it promising for $2e^-$ ORR: as the most Se rich compound in the Pd-Se phase diagram, $PdSe_2$ has a large Pd-Pd site separation (>4 Å in and out of plane) that helps to promote the selectivity for $2e^-$ ORR.[2] The dichalcogenide motif is also reminiscent of the dichalcogenide dumbells in the metal pyrite structures (e.g., CoS_2, $CoSe_2$, and $NiSe_2$) that have been demonstrated as highly active $2e^-$ ORR catalysts.[4,25,34] The

uncommon d^8 square-planar coordinated Pd embedded in a layered material is similar to the 2D metal organic frameworks (and SACs) that are active for $2e^-$ ORR in neutral media.[15,35,36] More broadly, several 2D electrocatalysts were recently identified as promising $2e^-$ ORR catalysts[37–39] and these compounds could be exfoliated from the bulk crystals for electrode fabrication.

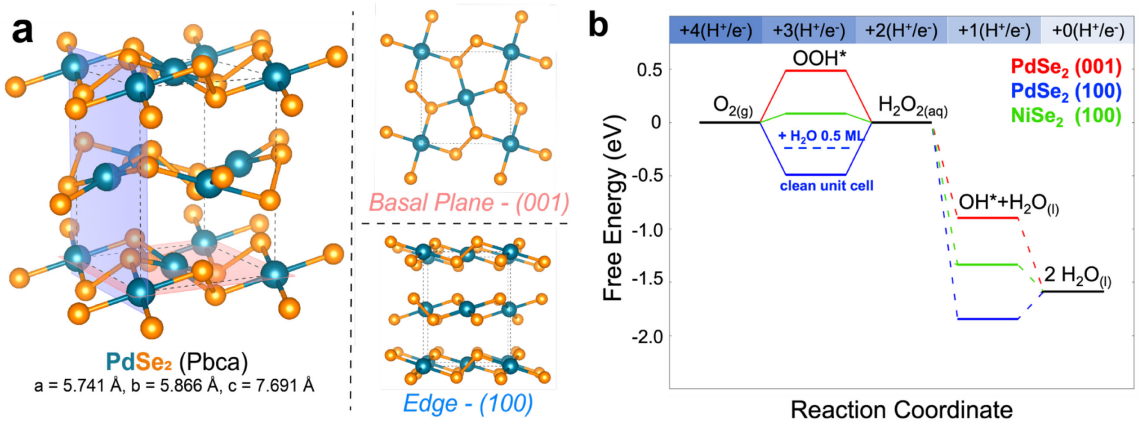

Figure 1. Crystal structure and theoretical calculations on 2D $PdSe_2$. a) Structure of $PdSe_2$ (left) with the (001) basal plane highlighted in pink and shown on the top right (as a monolayer for clarity) and the (100) plane highlighted in light blue and shown on the bottom right. b) Free energy diagrams of the reaction intermediates on $PdSe_2$ (001) and (100) surfaces at the calculated equilibrium potential with free energies of intermediates on $NiSe_2$ shown for comparison.[4] The dashed blue line represents OOH* in the presence of specifically adsorbed water (see Computational Methods for the validation of including a specifically adsorbed water molecule).

Here, we computationally and experimentally study 2D $PdSe_2$ and reveal its high catalytic activity and selectivity for the $2e^-$ ORR and good stability in neutral media. Theoretical calculations predict that both the basal plane and edge facets to be thermodynamically viable surfaces for $2e^-$ ORR, but with different kinetic behaviors. Electrochemical studies of hydrothermally synthesized $PdSe_2$ nanoplates demonstrate that 2D $PdSe_2$ is uniquely active and

selective for $2e^-$ ORR in neutral media over other crystalline Pd-Se phases. Effective bulk electrosynthesis of H_2O_2 in neutral media has been achieved using $PdSe_2$ catalyst supported on a gas diffusion electrode and the stability is confirmed by long-term electrolysis operation, elemental analysis of the electrolyte and various ex-situ and in-situ structural characterizations including synchrotron X-ray absorption spectroscopy (XAS).

RESULTS AND DISCUSSION

Prediction of $2e^-$ ORR Catalytic Behaviors on $PdSe_2$. Given the layered structure of $PdSe_2$, we expect that the dominant electrochemically active facets of interest will be the (100)/(200) edges and the (001)/(002) basal planes (Figure 1a). To understand the electrochemical stability of $PdSe_2$, we first calculated the surface Pourbaix diagrams of the $PdSe_2$ (001) and (100) surfaces (Figure S1 and Table S1-S2) by using the computational hydrogen electrode (CHE) method[40] under the assumption that the surfaces are in equilibrium with bulk water.[25] (Equation 1)

$$O_mH_n * + (2m - n)(H^+ + e^-) \rightarrow * + m\, H_2O_{(l)} \quad (1)$$

Particularly interesting is the fact that the two surfaces show very different trends in the stability of adsorbates. The (001) surface is predicted to be free of water-related reduction products over a wide range of electrode potential. On the other hand, the potential window for a "clean" (100) surface is predicted to be narrower, although it is predicted to persist under the relevant applied potential. Note that the Pd-Se bond breaking is not required to generate the basal (001) surface with only van der Waals interaction. On the other hand, generation of the (100) surface requires cleavage of Pd-Se bonds, which is expected to make this surface more reactive. Our calculations also suggest that specific adsorption of one water molecule per unit cell is favored on the (100) surface (-0.38 eV).

Next, we calculated the reaction free energy diagrams for $2e^-$ ORR on both surfaces at the calculated equilibrium potential using the CHE method (Figure 1b, Figure S2). Given the substantial differences in the stability of the (001) and bare, water-free, (100) surfaces, it is therefore not surprising that stability of OOH* varies significantly between the two surfaces; at the calculated equilibrium potential of $2e^-$ ORR, the first proton-coupled electron transfer (PCET) step (Equation 2) is uphill by 0.48 eV and downhill by 0.49 eV on (001) and (100) surfaces, respectively, whose magnitude determines the thermodynamic liming potential. Since the (100) surface features an equilibrium coverage of water molecules, we also found the adsorption energy of OOH* on the (100) surface is destabilized by ~0.3 eV in the presence of this adsorbed water (Fig. 1b dash line), leading to a substantial decrease in the predicted overpotential.

Because the standard reduction potential of $4e^-$ ORR (1.23 V) is higher than that of $2e^-$ ORR (0.69 V), the selectivity to H_2O_2 is determined by the competition between the kinetics of $2e^-$ and $4e^-$ ORR. To achieve a more comprehensive picture, we therefore considered the following PCET reactions,

$$O_{2(g)} + (H^+ + e^-) \rightarrow OOH* \quad (2)$$

$$OOH* + (H^+ + e^-) \rightarrow H_2O_{2(aq)} \quad (3)$$

$$OOH* + (H^+ + e^-) \rightarrow O* + H_2O_{(l)} \quad (4)$$

$$H_2O_{2(aq)} + (H^+ + e^-) \rightarrow OH* + H_2O_{(l)} \quad (5)$$

along with the following thermal (non-electrochemical) steps,

$$O_{2(g)} \rightarrow 2\,O* \quad (6)$$

$$OOH* \rightarrow O* + OH* \quad (7)$$

$$H_2O_{2(aq)} \rightarrow 2\,OH* \quad (8)$$

We used "constant-charge" calculations to estimate the barriers to the various PCET processes, reactions (2)-(8). Note that the calculated potentials of zero charge of the 3-layered (001) and 5-

layered (100) surfaces are around 0.3 V vs SHE, where all the steps involved in $2e^-$ ORR become downhill. The use of an implicit solvation model and a large supercell makes the shift in work function small throughout the reactions (see Computational Details for the validation of the constant-charge calculations). For the PCET processes, we expect the calculated energy barriers to be lower bounds to the true barriers, since the bulk protons will be further stabilized via additional hydration as compared to our interfacial model. Nonetheless, the relative PCET barriers can be safely compared to estimate the relative selectivity of various PCET processes.

On the (001) facet, reduction of O_2 to OOH* via PCET [reaction (2)] is expected to proceed with minimal to no barrier under the applied potential, and thus strongly outcompete thermal dissociation of O_2* [reaction (6)]. The resulting OOH* can again be reduced via PCET to H_2O_2 [reaction (3)], undergo reductive elimination via PCET [reaction (4)] or thermal dissociation to O* and OH* [reaction (7)]. Our results suggest that the PCET barrier for the reduction to form H_2O_2 is at least 0.3 eV lower than that for reductive elimination, which in turn is smaller than the barriers for thermal dissociation. The same considerations also hold for the (100) surface, suggesting a high selectivity on that surface as well. As such, even in the absence of a detailed microkinetic model, high selectivity to H_2O_2 should be expected, however with perhaps higher activity on the (100) relative to (001) given the reduced thermodynamic limiting potential.

Beyond the initial formation of H_2O_2, we also need to consider the possible reduction of the accumulated H_2O_2 both at the electrode surface and in bulk solution, because it ultimately limits the highest achievable concentrations of H_2O_2.[7] Here, it is important to note that the adsorption free energy of $H_2O_{2(aq)}$ highly depends on the surface, varying from 0.28 eV to -0.12 eV on the (001) and (100) surfaces, respectively. Once readsorbed, the H_2O_2 can be consumed via both reductive elimination [reaction (5)] or thermal dissociation [reaction (8)] (see these barriers

in Table S3 and S4). In contrast to the "inert" (001) surface, both thermal dissociation and reductive elimination of H_2O_2 appear quite feasible on the (100) surface, and thus could limit the accumulation of $H_2O_{2(aq)}$.

Synthesis and Characterization of $PdSe_2$ Nanoplates. We synthesized $PdSe_2$ nanoplates using a facile hydrothermal reaction of palladium chloride and selenourea in near-stoichiometric ratios (see Materials and Methods for details). The powder X-ray diffraction pattern (PXRD) of the product matched the standard pattern of pentagonal 2D $PdSe_2$ (Figure 2a) without major impurities from other known Pd-Se phases. Scanning electron microscopy (SEM) images show that the $PdSe_2$ product has a rectangular nanoplate-like morphology with typical lateral dimension of 200-2000 nm, with enriched surface area in the (001) basal plane compared to the (100) edges (Figure 2b). Transmission electron microscopy (TEM) images (Figure 1c, Figure S3) also show the morphology of the nanoplates. Furthermore, the indexed selected area electron diffraction (SAED, Figure 1d) along the [001] zone axis confirms the orientation of the plates lying flat on the TEM grid is perpendicular to the [001] crystallographic direction. This shows that the major exposed facet of these $PdSe_2$ plates lying parallel to the substrate is the (001) basal plane, which also means that the other edges of the rectangularly shaped plates correspond to the (100) edge facets. The Raman spectrum matched with that previously reported[30] for bulk $PdSe_2$ (Figure 2e), confirming that the these nanoplates do not approach few-layer thicknesses. Therefore, these $PdSe_2$ nanoplates should have metallic behavior, rather than the large bandgaps expected for near-monolayer $PdSe_2$,[30] which should be beneficial for electrocatalysis. Energy dispersive spectroscopy (EDS) via SEM showed a slightly less than ideal Se/Pd ratio of 1.6 from mapping results. More careful point-by-point EDS analysis of individual nanoplates (Figure S4) showed an average Se/Pd ratio of 1.7 ± 0.2. From a bulk elemental analysis by inductively coupled plasma optical emission

spectroscopy (ICP-OES) measurements of digested samples we found the Se/Pd ratio to be 1.98. This suggests that the deviation of the EDS analysis is likely due to typical errors intrinsically associated with EDS without standardization and its relatively small sampling size. X-ray photoelectron spectroscopy (XPS) on the as-synthesized $PdSe_2$ powder suggested the surfaces of the nanoplates were more Se rich (Figure S5). Since $PdSe_2$ is the most Se rich phase in the Pd-Se phase diagram, this could be due to the potential residual elemental Se on the surface from the synthesis process.

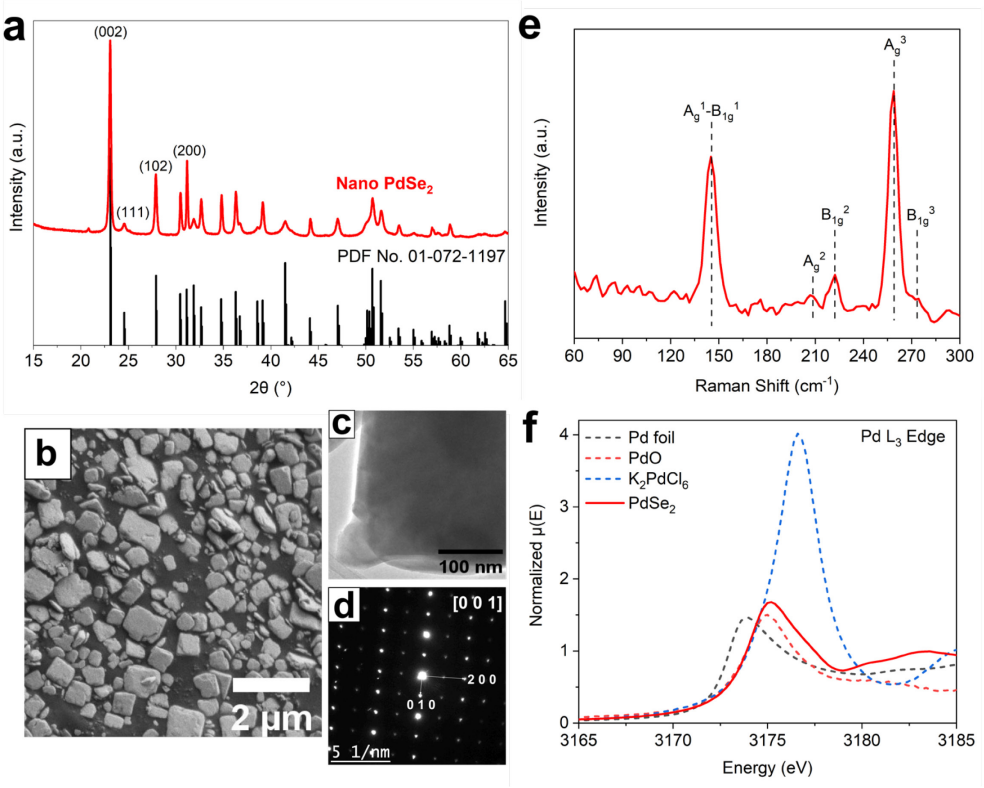

Figure 2. Structural characterization of as-synthesized $PdSe_2$ nanoplates. a) Powder X-ray diffraction pattern of $PdSe_2$ compared to the standard pattern of orthorhombic $PdSe_2$ (PDF No. 01-072-1197). b) SEM micrograph of $PdSe_2$ nanoplates. c) TEM micrograph of a $PdSe_2$ plate viewed down the [001] zone axis and d) the corresponding indexed SAED pattern. e) Raman spectrum of

$PdSe_2$ with previously calculated Raman modes overlaid. f) Pd L_3 edge XANES of $PdSe_2$ in comparison with Pd foil, PdO, and K_2PdCl_6 as oxidation state standards.

To elucidate the electronic structure of the probable ORR active sites of $PdSe_2$, we conducted X-ray absorption spectroscopy X-ray absorption near edge spectroscopy (XANES) at the Pd L_3-edge (Figure 2f, Figure S6). The position of the white line and the white line intensity for $PdSe_2$ are most similar to that of PdO (Pd^{2+}), falling between the intensities/edge positions of Pd foil (Pd^0) and K_2PdCl_6 (Pd^{4+}), suggesting that the oxidation state of Pd in $PdSe_2$ is close to +2. Se K-edge XANES (Figure S7d) show similarity in peak shapes to Se_2^{2-} in $CoSe_2$,[25] further confirming that $PdSe_2$ and pyrite phase $CoSe_2$ have similar Se-Se dumbbells. XANES at the Pd L_2-edge similarly matched a Pd^{2+} oxidation state (Figure S6) for $PdSe_2$. For comparison, we also synthesized nanomaterials of tetragonal Pd_4Se and cubic $Pd_{17}Se_{15}$ without major impurities using similar hydrothermal methods (Figure S8). $Pd_{17}Se_{15}$ also has a similar oxidation state, while Pd_4Se exhibits an oxidation state between Pd(0) and Pd(I) (Figure S6). SEM images of the $Pd_{17}Se_{15}$ and Pd_4Se products (Figure S9) reveal a high surface area morphology suitable for electrocatalysis, although without well-defined faceting.

$2e^-$ ORR Activity and Selectivity of $PdSe_2$. To evaluate the $2e^-$ ORR activity, selectivity, and stability of $PdSe_2$, we first conducted electrochemical tests using a rotating ring disk electrode (RRDE) in a neutral buffer solution (0.05 M NaPi = 0.025 M Na_2HPO_4/0.025 M NaH_2PO_4, pH = 6.8-6.9). A high selectivity for $2e^-$ ORR above 80% can be maintained across a large overpotential window (Figure 3a blue curve) for suitable catalyst loading. If we would like to optimize the $2e^-$ ORR catalytic performance, a high ring current of >1 mA/cm^2_{disk} was observed at high overpotential (~0.2 V vs. RHE), and the selectivity remained >60% at the peak ring current (Figure 3a cyan curve) for higher effective mass loading. In comparison, RRDE measurements of Pd_4Se

and $Pd_{17}Se_{15}$ further illustrate the unique behavior of $PdSe_2$ in the family of crystalline Pd-Se phases: even though all three Pd-Se phases exhibit significant catalytic activity in neutral solutions, only $PdSe_2$ displays high selectivity for $2e^-$ ORR (Figure 3b). In contrast to other metal compound $2e^-$ ORR electrocatalysts, the activity of $PdSe_2$ in buffered neutral conditions and that in acidic conditions are quite similar (Figure S10), and the high selectivity is maintained in both pH conditions at potentials up to 0.05 V vs. RHE.

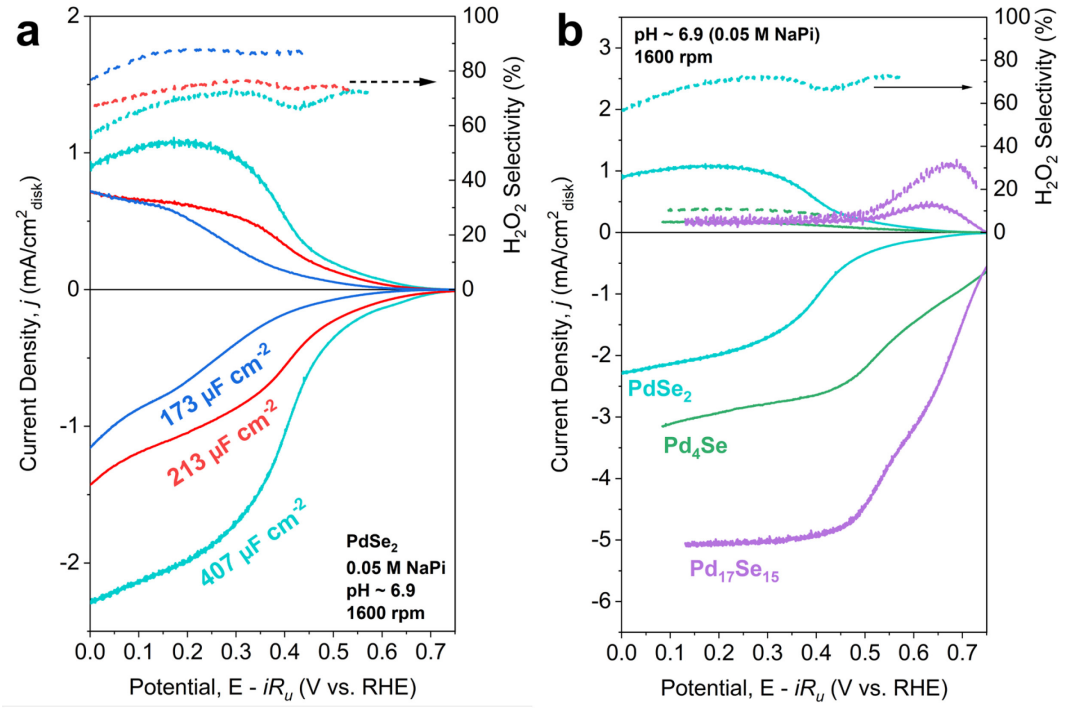

Figure 3. a) Representative rotating ring disk electrode (RRDE) measurements of the catalytic properties of $PdSe_2$ nanoplates with various mass loadings in O_2-saturated conditions with 0.05 M NaPi buffer (pH ~ 6.9) and a rotation rate of 1600 rpm, and b) in comparison with other Pd-Se phases (Pd_4Se and $Pd_{17}Se_{15}$) at the same catalyst mass loading. The top solid traces represent the

ring current density (normalized to the geometric area of the disk) and the bottom traces represent the disk current density. Dashed traces represent selectivity (right axis).

Even though selectivity remained high across many samples, the ring current was found to be highly dependent on the double layer capacitance (C_{dl}) which is proportional to surface area (Figure S11-S13) and ultimately determined by catalyst mass loading. Although this effect is observed for other metal compound catalysts,[18,34] it is more drastic in 2D $PdSe_2$ possibly due to the additional dependence of edge vs. basal plane exposure.[41] Since RRDE samples depend on the dispersion of the catalyst films as well as the edge/basal plane ratio in the catalyst dispersion, the mass loading, resultant capacitance, and thus the observed activity/selectivity can be highly variable for similar mass loadings.

Bulk Electrosynthesis of H_2O_2 on $PdSe_2$. To evaluate the practical performance of $PdSe_2$ for electrosynthesis of H_2O_2, we prepared a gas diffusion electrode (GDE) loaded with $PdSe_2$ catalyst (Figure 4a) and applied a constant current in a two-compartment flow cell to rapidly accumulate H_2O_2 (see Methods and Figure S14 for details). We initially measured CV on the $PdSe_2$/GDE electrode and observed a cathodic current onset of ~0.6 V vs. RHE, and a large increasing current up to almost -90 mA (or -16 mA cm^{-2}) at 0 V vs. RHE (Figure 4b).

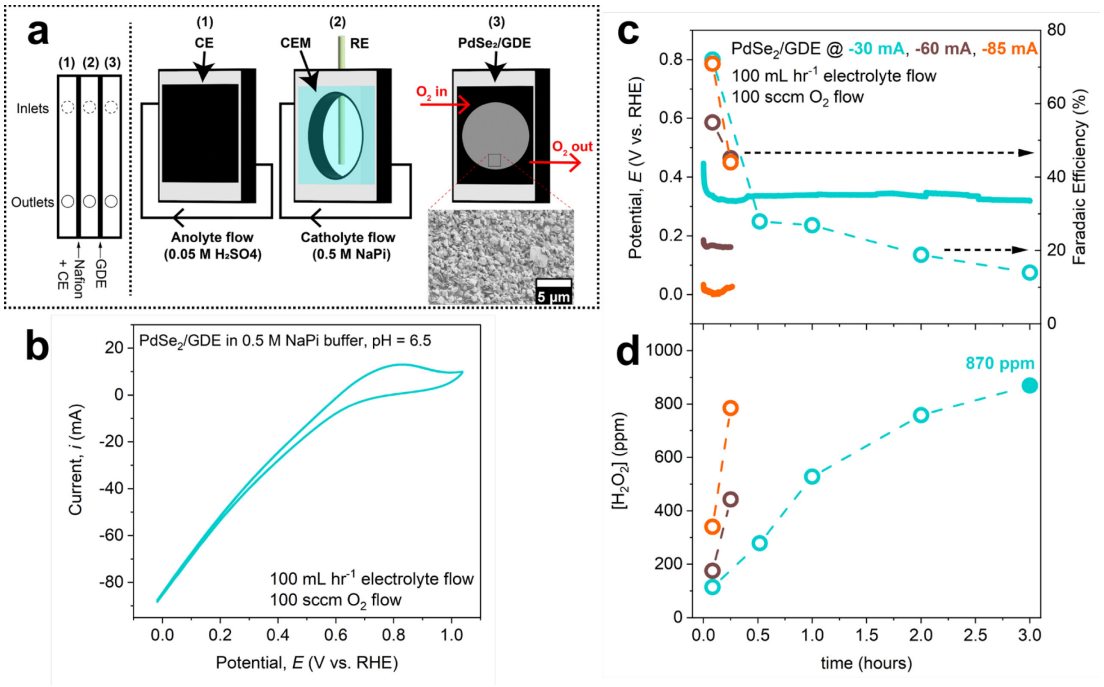

Figure 4. Electrosynthesis of H_2O_2 in a flow cell on a $PdSe_2$/GDE electrode. A constant current of -30 mA (-5 mA cm^{-2}), -60 mA (-10 mA cm^{-2}), and -85 mA (-15 mA cm^{-2}) in a buffer solution of 0.25 M Na_2HPO4/0.25 M NaH_2PO_4 (initial pH ~ 6.5). a) Schematic of the 3-layer GDE/flow-cell assembly with each layer annotated and a representative SEM image of the $PdSe_2$ catalyst dispersed on GDE electrode. b) Cyclic voltammogram of the $PdSe_2$ loaded GDE before the electrosynthesis process, c) potential vs. time curve (continuous line, left-axis) and Faradaic efficiency (dots, right axis) of the $PdSe_2$/GDE during constant current electrosynthesis, and d) the corresponding H_2O_2 accumulation during the H_2O_2 electrosynthesis processes.

Based on the CV, we performed an extended electrosynthesis test at a fixed current of -30 mA (Figure 4c cyan curves). After an initial onset curve, the potential remained fairly constant at ~0.3 V vs. RHE over a 3-hour electrolysis, and yielded an accumulated H_2O_2 concentration of 870 ppm (Figure 4d, cyan curve). Rapid accumulation of H_2O_2 was also achieved over the $PdSe_2$/GDE electrode at constant currents of -85 mA and -60 mA (Figure 4c,d and Figure S15) allowing for

accumulation of a similar amount of H_2O_2 (785 ppm) in just 15 minutes with a Faradaic efficiency of >50% and a potential of ~0 V vs. RHE. After the electrosynthesis, the final pH remained near neutral for all measurements.

The drop in Faradaic efficiency over the duration of bulk electrolysis is similar to that observed for cubic $NiSe_2$.[4] To understand this, we comprehensively considered both the production and decomposition of the H_2O_2 and also computationally compare the expected catalytic properties of 2D pentagonal $PdSe_2$ against those of pyrite phase $NiSe_2$ with a cubic symmetry and identical (100) and (001) surfaces (Figure 1b). $NiSe_2$ is predicted to be more active than the $PdSe_2$ based on the stability of OOH* (Figure 1b). The $PdSe_2$ (100), $PdSe_2$ (001), and $NiSe_2$ surfaces each have large barriers for the thermal bond dissociation of OOH* [reaction (7), Table S3], which is beneficial for $2e^-$ ORR. Since both $PdSe_2$ (100)/(001) and $NiSe_2$ show barrierless PCET steps for $2e^-$ ORR with larger barriers for reaction (4), both should favor $2e^-$ ORR over $4e^-$ ORR. However, the barrier for the further reduction of H_2O_2 [reaction (5)] over $NiSe_2$ lies between those of $PdSe_2$ (100) and $PdSe_2$ (001) surfaces (Table S4), which can be explained by the trend of the relative stability of OH* to H_2O_2* (or the Brønsted-Evans-Polanyi (BEP) principle). Therefore, the $PdSe_2$ (001) surface is expected to demonstrate better selectivity and accumulation of H_2O_2, and the kinetic behavior of $NiSe_2$ and $PdSe_2$ (100) edges may dictate the overall Faradaic efficiency of electrosynthesis over these surfaces.

Notably, the $PdSe_2$/GDE electrosynthesis performance is highly dependent on the loading and morphology of the deposited catalyst film – a $PdSe_2$ film with higher loading on the GDE severely limited the Faradaic efficiency and accumulation of H_2O_2 during electrolysis (Figure S16). This was most likely due to inhibited O_2 transport to the triple phase boundary. Despite this, all GDE flow cell electrosyntheses resulted in significantly more H_2O_2 accumulation in a much

shorter time than a traditional H-cell electrosynthesis (Figure S17), which highlights the importance of cell design in evaluating the performance of $2e^-$ ORR catalysts. Full results of various electrosynthesis runs on the same electrode are summarized in Table S5 and also compared to the reported accumulation of H_2O_2 over various other $2e^-$ ORR catalysts in neutral media in Table S6. The high H_2O_2 production rate (7.9 mol $g_{catalyst}^{-1}$ h^{-1}) at 0 V vs. RHE is notably among the highest to reach practically useful concentrations of H_2O_2 in a conventional flow cell device.

Ex-situ and In-situ Studies on the Stability of $PdSe_2$. To confirm the predicted stability of $PdSe_2$, we conducted several post-electrolysis characterization experiments. First, in order to evaluate the viability for direct applications of the produced H_2O_2 where the concentrations of leached metal and Se must be low (i.e. wastewater treatment, semiconductor cleaning), we used ICP-OES to measure the amount of Pd and Se leached into the electrolytes during GDE electrosynthesis conducted with applied constant currents of -30 mA, and -60 mA, and -85 mA (Figure 5a). The leaching of Pd into the solution from the $PdSe_2$ catalyst was negligible at all measured operating currents, but the leaching rate increased with increasing current density from 0.05 ± 0.05 μg g_{cat}^{-1} h^{-1} at -30 mA to 0.5 ± 0.5 μg g_{cat}^{-1} h^{-1} at -85 mA. The Se leaching rate at an operating current of -30 mA (12.4 ± 0.5 μg g_{cat}^{-1} h^{-1}) was higher than that of Pd. Additionally, we compare several other metrics of stability across metal chalcogenide catalysts under different operating currents (Table S9). One such stability metric is an adaption of the "stability number" (S-number) previously defined for OER catalysts,[42] which we define as the molar ratios of the produced H_2O_2 to leached metal or Se. We find that $PdSe_2$ has a substantially higher metal S-number than $NiSe_2$ (~10^5 vs. ~10^3), and $PdSe_2$ and $NiSe_2$ have Se S-numbers on the same order of magnitude (~600 to ~900 depending on conditions).

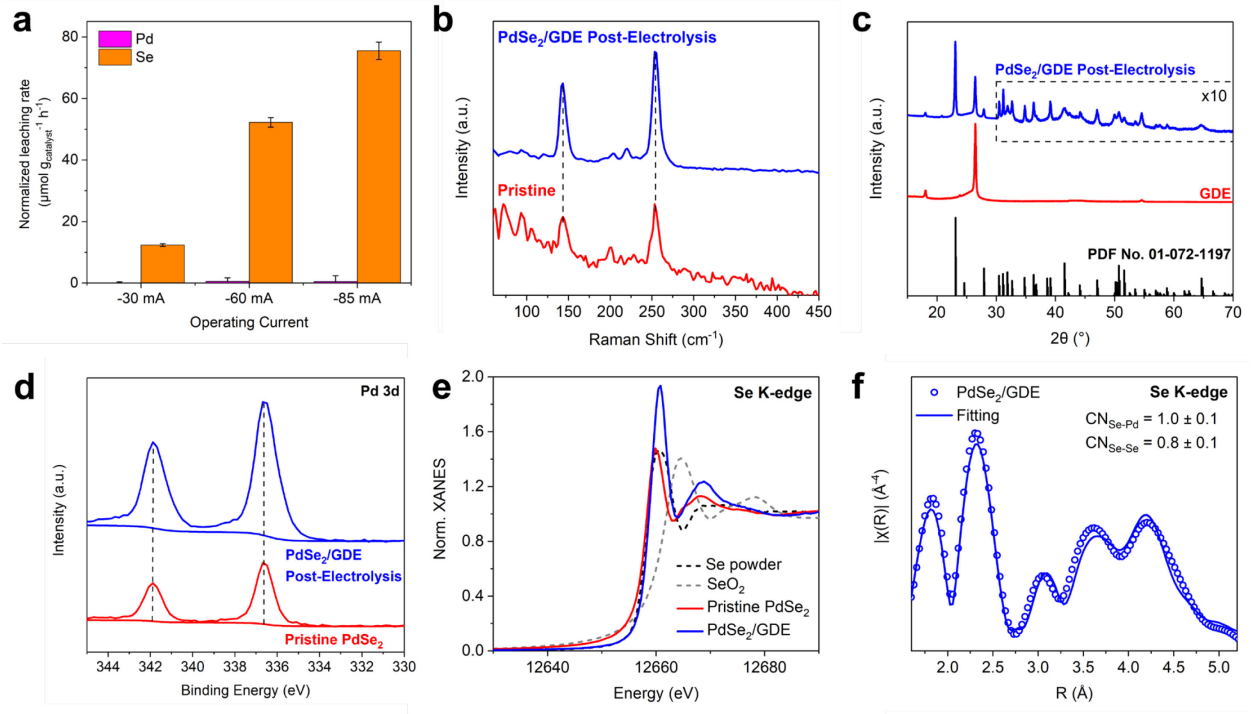

Figure 5. Electrochemical stability of $PdSe_2$ catalyst evaluated by various post-electrolysis chemical and structural characterizations. a) Leaching rates of Pd and Se in electrolytes measured by ICP-OES after electrosynthesis of H_2O_2 for 3 hours at –30 mA, 15 minutes at –60 mA, and 15 minutes at –85 mA. b) Raman spectra, c) XRD (after washing, peak intensities beyond $2\theta = 30°$ multiplied by 10 for visibility), d) XPS, e) XANES (fluorescence mode signal), and f) EXAFS (transmission mode signal) of the $PdSe_2$/GDE electrode after several electrosynthesis tests (as described in Figure 4 and Table S5) in comparison to the pristine $PdSe_2$ sample.

We then investigated the chemical stability of the $PdSe_2$ catalyst. Very little change was observed in the post-electrolysis Raman spectrum (Figure 5b, Figure S18), showing that the catalyst surface structure is largely maintained. Given the previously observed dependence of the Raman spectrum on $PdSe_2$ layer number,[43] this also suggests that $PdSe_2$ does not significantly delaminate. The XRD pattern of the $PdSe_2$/GDE after the electrolysis and rinsing with nanopure water closely matched a combination of the XRD patterns of $PdSe_2$ and the bare GDE (Figure 5c).

X-ray photoelectron spectroscopy (XPS) indicated that the valence states of Pd (Figure 5d) remained unchanged, suggesting that the Pd^{2+} active sites maintained their surface electronic environment. While there were minor changes to the Se XPS (Figure S19), these changes did not suggest formation of SeO_2, which was observed for other metal chalcogenides.[25] Furthermore, the peak shifts of the Pd 3d and Se 3d XPS due to partial oxidization of $PdSe_2$ were not observed. Similarly, the Pd-O bond[44] was not observed in the extended Raman spectrum (Figure S18) for both pristine $PdSe_2$ powder and the post-electrosynthesis $PdSe_2$/GDE electrode. The XPS measurements revealed the Se:Pd ratio decreased post-electrolysis, but was still in excess of a 2:1 ratio (Table S10), thus precluding the formation of $Pd_{17}Se_{15}$ triggered by Se leaching.[43] These results confirm that the active site for $2e^-$ ORR is indeed the square planar Pd^{2+} motif, rather than the higher valent Pd or Pd-O bonds formed due to oxidation, as observed for other $2e^-$ ORR catalysts.[21]

To further investigate the changes to the electronic structure of Se, we conducted ex-situ X-ray absorption spectroscopy (XANES) at the Se K-edge (see Methods). The similar ratio between the main white line peak and the post-white line peak (at ~12660 eV and ~12770 eV) confirms that Se remains anionic in character and precludes the formation of bulk Se oxides. Namely, the peak near 12770 eV was still clearly present, unlike in Se(0) powder, and cationic Se compounds (such as SeO_2) which show a clearly blue shifted white line peak. Additionally, the Se K-edge extended X-ray absorption fine structure (EXAFS) spectroscopy of post-electrosynthesis $PdSe_2$/GDE showed little change in the first two major peaks (Figure 5f). Fitting the EXAFS data (see details in Methods and Table S11 and S12) suggested a minimal decrease in Se-Se coordination (from 1 to 0.8 ± 0.1) but larger decreases in direct Se-Pd coordination (from 2 to 1.0 ± 0.1) and Se-Pd interlayer coordination (from 1 to 0.3 ± 0.1). Similar results were achieved with

a simplified fitting model (Table S11). Given the Se-rich samples and the lack of significant Pd leaching, these changes in Se-Pd paths could be indicative of some subtle local restructuring of the Pd sites that does not disrupt the overall layered motif of the $PdSe_2$ catalyst.

To further confirm the operational stability of $PdSe_2$ catalyst on a longer timescale, we fabricated a GDE electrode with a high loading of Nafion to prevent electrolyte flooding through the gas diffusion electrode. The absolute current observed (Figure S20a) was similar to that of other $PdSe_2$/GDE electrodes measured. By tuning the catalyst microenvironment, we could continuously operate the $PdSe_2$/GDE electrode for 48 hours at -75 mA to accumulate more than 600 ppm of H_2O_2 (Figure S20b). In fact, the device operation was only stopped due to the overload at the OER counter electrode. Even after this much longer operation time, the $PdSe_2$ catalyst retained high S-numbers of 2.07×10^4 for Pd and 416 for Se. Such long term operational catalyst stability suggests that the H_2O_2 concentration buildup is likely the primary mechanism of Se leaching from $PdSe_2$. This high stability would enable repeated use of the $PdSe_2$ catalyst in separate solutions, or in a single pass flow cell configuration. After several tests, this $PdSe_2$/GDE electrode was digested for ICP-OES measurement, which showed a decrease of the Se:Pd ratio from 1.98:1 (as measured in the pristine electrode) to 1.30:1 (Table S10). Taken together with the more surface sensitive XPS/EDS results (Table S10) and the bulk sensitive EXAFS results (Figure 5f), this further suggests differences between the catalytic active surface and the bulk of the $PdSe_2$ catalyst triggered by faster Se loss.

After confirming ex-situ that $PdSe_2$ maintained its bulk structure and valence states after electrolysis, we also sought to probe the dynamic electronic and local structure changes under the operating conditions of $2e^-$ ORR using in-situ XAS (see details in Methods and Figures S7 and S21). Interestingly, the Pd and Se K-edge XANES peak shapes and edge positions were unchanged

from open circuit potential (E_{OC}) up to a potential of 0 V vs. RHE (Figure S7c and S7d). This suggests that there is no substantial adsorption of oxygenates on the Se sites. Furthermore, Se K-edge EXAFS exhibited very minimal changes in peak intensities or positions under similar conditions (Figure S7e and S7f), indicating no major changes to the local structure of $PdSe_2$ under operating conditions. These in-situ experiments further confirm that the $PdSe_2$ catalyst is stable with minimal local structure changes under ORR operating conditions and high concentrations of H_2O_2.

CONCLUSIONS

In conclusion, our joint computational and experimental study shows crystalline 2D pentagonal $PdSe_2$ to be an active and stable $2e^-$ ORR electrocatalyst for electrosynthesis of H_2O_2 in neutral solutions. Computational free energy diagrams reveal both the basal plane and edge of $PdSe_2$ nanoplates to be active and selective towards $2e^-$ ORR but with different surface speciation in solution and H_2O_2 degradation kinetics. Hydrothermally synthesized nanoplates of $PdSe_2$ can achieve >1 mA/cm^2_{disk} ring currents in RRDE measurements while maintaining high selectivity at high overpotentials, which is significantly better than other crystalline Pd-Se phases examined (Pd_4Se and $Pd_{17}Se_{15}$). Using gas diffusion electrodes loaded with the $PdSe_2$ catalyst, >800 ppm of H_2O_2 can be electrochemically synthesized in buffered neutral solution within 3 hours using a constant current procedure, or even more rapidly (15 min) at larger current densities/overpotentials. After bulk electrolysis, analysis of the electrode via XRD, Raman, and XPS confirmed that $PdSe_2$ maintains its structure, and ICP-OES analysis of the operation solutions showed negligible Pd loss and slow Se loss. The $PdSe_2$/GDE electrode can be continuously operated under a constant current in a flow cell for at least 48 hours. Ex-situ and in-situ XANES and EXAFS measurements of the $PdSe_2$/GDE confirm subtle changes around the Se sites and

stability over a wide potential range during ORR electrolysis conditions. We anticipate that further tuning of the edge/basal plane ratio by using facet-selective growth or exfoliation could further tune the catalytic properties of $PdSe_2$. This work establishes a stable electrocatalyst with a unique pentagonal structural motif to achieve rapid practical electrosynthesis of H_2O_2, opening up further studies of a new and unique class of 2D electrocatalysts.

EXPERIMENTAL SECTION

Computational methods

The Vienna Ab initio Simulation Package (VASP)[45,46,47] interfaced with the Atomic Simulation Environment (ASE)[48] was used for energies and geometry optimization for all adsorbates. The core electrons are described by projector augmented wave (PAW) pseudopotentials[49] and the Perdue-Burke-Ernzerhof (PBE)[50] functional was used to treat exchange and correlation. The Tkatchenko-Scheffler(TS) method[51] was utilized to treat dispersion because PBE-TS method is known to give reasonable lattice constants of bulk $PdSe_2$[52]. Note that PBE-D3 method was used for the $NiSe_2$ system.[4] Each electronic self-consistent field (SCF) calculation was converged below 10^{-5} eV and the surface adsorbates were allowed to relax until forces became below 0.01 eV/Å. Solvation effects are described by using the implicit solvation model, VASPsol[53,54]. The effective surface tension is set to zero due to the numerical stability[55,56], which is validated by the fact that the difference in adsorption energy between the default value (0.525 meV/Å^2) and 0 meV/Å^2 is less than 0.01 eV. The Brillouin zone was sampled using 10×10×10, 10×10×1, and 10×8×1 Γ-centered Monkhorst-Pack mesh[57] for bulk, (001), and (100) facets calculations, respectively. When larger supercells were used, the corresponding Brillouin zones were sampled. The (001) surface of $PdSe_2$ was modeled as a 4-layered 1×1 unit cell slab with two bottom layers fixed, which

corresponds to 8 Pd atoms and 16 Se atoms. The (100) surface was modeled as a 5-layered 1×1 unit cell slab with two bottom layers fixed, which corresponds to 10 Pd atoms and 20 Se atoms. The choice of the number of layers was validated by the convergence of adsorption energies of O*, OH* and OOH* with respect to the number of layers. For the electrochemical activation barrier calculations, 3-layered $PdSe_2$ (001) slabs and 4-layered (100) slabs were used for efficiency. Since simple implicit solvation is unable to capture the steric and electronic interactions with such adsorbed water,[58] we included also one specifically adsorbed water in our subsequent calculations and confirmed that the presence of the adsorbed water does not change the conclusion although the stability of intermediates could be changed a little bit.

The free energy of $H_2O_{(l)}$ was calculated using the experimental free energy difference between $H_2O_{(l)}$ and $H_2O_{(g)}$. The free energy of O_2 was determined by setting it to give the experimental standard reduction potential (1.229 V) of the reaction, $0.5\ O_{2(g)} + H_2 \rightarrow H_2O_{(l)}$. The free energies of adsorbates were calculated using $G = E_{DFT} + U_{thermal} + ZPE - TS$, where E_{DFT} is the energy obtained from DFT calculations, $U_{thermal}$, ZPE and S are the contribution from thermal internal energy, the zero-point energy, and entropy, respectively, which are calculated under the harmonic approximation. The free energies of gas-phase/aqueous H_2O_2 are calculated by using Gaussian 16[59] with the SMD continuum solvation model[60]. The calculated standard reduction potential of $2e^-$ ORR is 0.83 V, which is slightly higher than the experimental value (0.69 V) and close to other computed values.[25,34]

The proton-coupled electron transfer (PCET) reaction of a general adsorbate can be written as:

$$A* + (H^+ + e^-) \rightarrow AH* \qquad (9)$$

The electrochemical potentials of a proton and an electron pair were calculated by using the computational hydrogen electrode (CHE) method[40] (Equation 10):

$$\widetilde{\mu_{H^+}} + \widetilde{\mu_{e^-}} = 0.5\,\mu_{H_2} - U_{RHE} \qquad (10)$$

where $\widetilde{\mu_{H^+}}$ and $\widetilde{\mu_{e^-}}$ are the electrochemical potentials of a proton and an electron, and μ_{H_2} is the chemical potential of hydrogen gas at the standard state, and U_{RHE} refers to the applied potential vs RHE. Transition states for thermal bond dissociation were searched using the nudged elastic band (NEB)[61] method and the dimer method[62]. The Eigen ion ($H_9O_4^+$) was used as a model for a solvated proton for an electrochemical process because the use of the Eigen ion was validated for HER on Pt.[63] Furthermore, because the purpose of this calculation is the comparison of activation energy, we believe it is safe to rely on the static minimum energy path and ignore the solvent fluctuations and entropic effects, which are normally avoided by considering a backward barrier and adding the reaction free energy obtained from the CHE method to avoid the description of a solvated proton at the interface.[64] By using the nudged elastic band (NEB) method[61] and the dimer method[62], we calculated the "constant-charge" activation energy, not constant-potential activation energy. We believed it is sufficient to consider just the "constant-charge" activation energy to compare competing PCET steps because the competing steps are likely to experience similar electrochemical environments.[65] This is particularly important for the (001) surface because the (001) surface has a non-zero band gap, i.e., the assumption of the simple capacitor model cannot be valid, and furthermore, its potential of zero charge (PZC) or work function, which is important to convert a constant charge barrier into a constant potential barrier, highly depends on the interlayer distance, which is also highly sensitive to the presence of the dispersion correction method. Fortunately, the comparison of the $PdSe_2$ (100), $PdSe_2$ (001), and $NiSe_2$ surfaces with the constant charge barriers can be reasonable by the fact that the calculated work function values of

the range between 4.5 to 4.8 eV, which implies that the adsorbates experience similar electrochemical conditions during PCET processes. In addition, we believe the trend remains the same even if the proton donor changes from a solvated proton to water.

Chemicals and materials. Palladium chloride (≥99.9%) was obtained from Sigma-Aldrich. Selenourea (98+%) was obtained from Acros Organics. Carbon fiber paper (CFP, Toray: 5% wet proofing) was obtained from Fuel Cell Earth and plasma treated and heated at 700 °C in air for 5 minutes prior to use. Sigracet 28 BC gas diffusion electrodes (GDE) were used for all GDE electrosynthesis measurements.

Materials synthesis. The $PdSe_2$ nanoplates were synthesized by a hydrothermal method. Briefly, 1.0 mmol of $PdCl_2$ (0.18 g) and 2.0 mmol selenourea (0.25 g) were dissolved in 9 mL of nanopure water and added to a Teflon lined 20 mL stainless steel autoclave. The autoclave was sealed and heated at 220 °C for 12 hours and allowed to cool in air. The resulting powder was washed with nanopure water and ethanol before being dried under vacuum at 60 °C. Nanoparticles of Pd_4Se and $Pd_{17}Se_{15}$ were synthesized by similar methods with appropriate stoichiometric amounts of $PdCl_2$ and selenourea.

Materials characterization. Powder X-ray diffraction (PXRD) patterns were collected on a Bruker D8 ADVANCE powder X-ray diffractometer using Cu Kα radiation with a 0.6 mm slit. Scanning electron microscopy (SEM) images were collected on a Zeiss SUPRA 55VP field emission scanning electron microscope at a typical accelerating voltage of 1-3 kV for imaging. Electron dispersive spectroscopy (EDS) spectra were collected on the same microscope using an accelerating voltage of 22 kV and a Thermo Scientific UltraDry EDS Detector, and the Pd and Se L-lines were used for quantification. X-ray photoelectron spectroscopy (XPS) was performed on a Thermo Scientific K-Alpha XPS system with an Al Kα X-ray source. Raman spectra were

collected on a ThermoFisher Scientific DXR3xi Raman imaging microscope using a 532 nm laser with a 10 mW laser power. Transmission electron microscopy (TEM) imaging was performed on a FEI Tecnai TF-30 TEM instrument (300 kV). The $PdSe_2$ nanoplates were dispersed in nanopure water with a concentration of 2.5 mg/mL and dropcast onto lacey carbon supported Cu TEM grids (TEM-LC200CU25, Sigma-Aldrich).

XAS experiments and data analysis. X-ray absorption spectroscopy (XAS) was collected at beamlines 10-ID (Pd K-edge, Se K-edge) and beamline 9-BM (Se K-edge, Pd $L_{2,3}$-edge), and 20-BM (ex situ Se K-edge data on $PdSe_2$/GDE) of the Advanced Photon Source. XAS data were collected in fluorescence mode with an ion chamber detector for data from 10-ID, a Vortex silicon drift detector for the Pd $L_{2,3}$-edge, a Passivated Implanted Planar Silicon (PIPS) detector for the Se K-edge (at 9-BM), a 13-element Ge detector for Se K-edge data at 20-BM in fluorescence mode, and by ion chamber for transmission mode data (collected simultaneously on ex situ samples at 20-BM). Pd $L_{2,3}$-edge spectra were collected in a He-purged sample chamber. Ex situ measurements on $PdSe_2$/GDE were collected in transmission mode. XAS data were analyzed in Athena using an R_{bkg} of 1 and a Hanning window with a k-range of 3-12 and dk = 1. EXAFS fitting was completed in Artemis and the S_0^2 value was obtained by fitting pristine $PdSe_2$ with fixed coordination numbers while other parameters were allowed to vary. For subsequent fitting of the $PdSe_2$/GDE data, the S_0^2 was fixed while all other parameters were allowed to vary.

Rotating ring disk electrode preparation and measurements. Rotating ring-disk electrodes (RRDE, Gaoss Union, 4 mm disk diameter) were polished successively with 1, 0.3, and 0.05 μm alumina suspensions (Allied High Tech Products) on polishing pads (Buehler, MicroCloth), and subsequently rinsed with nanopure water before brief (~20 seconds) sonication in ethanol then quickly blow drying with N_2. The catalysts were made into dispersions with a 1:9 v:v mixture of

Nafion solution (5 wt%, Sigma-Aldrich) and water then drop-casted onto the RRDEs with various amounts of catalyst loading. RRDE measurements were conducted in an undivided cell using a Bio-Logic VMP3 potentiostat with a graphite rod as the counter electrode and a Hg/Hg_2SO_4 reference electrode (CHI151, CH Instruments Inc.) that was calibrated against a saturated calomel electrode (CHI150, CH Instruments Inc.). The cell contained approximately 45 mL of neutral buffered electrolyte (0.025 M Na_2HPO_4/0.025 M NaH_2PO_4 = 0.05 M NaPi, pH ~ 6.9, which was pre-purged with Ar or O_2 gas before measurements, and then the corresponding gas was kept in the headspace of the solution for the duration of the measurement. During RRDE measurements, the ring was typically held at 1.3 V vs. RHE (pre *iR* correction) where H_2O_2 reduction is diffusion limited. The H_2O_2 selectivity was then calculated according to the follow equation:

$$H_2O_2\ Selectivity\ (\%) = \frac{200(\frac{I_{ring}}{N})}{\frac{I_{ring}}{N} + I_{disk}}$$

Where *N* is the collection efficiency of the ring, which was calibrated by the ring/disk current ratio during ferricyanide reduction. Disk current measured under Ar-saturation was subtracted from the LSVs measured under O_2-saturation. The double layer capacitance, C_{dl}, was calculated by measuring CVs at different scan rates under Ar-saturation and taking the slope of the difference between anodic and cathodic scan rates at a specific potential vs. scan rate (Figure S11). *iR* correction was performed manually by measuring the uncompensated resistance (R_u) from electrochemical impedance spectroscopy (EIS) at the open circuit potential.

Flow cell electrosynthesis measurements. Bulk electrosynthesis experiments were conducted in a custom-made flow cell (Figure S14) with a leakless Ag/AgCl reference electrode (Innovative Instruments, LF-1) inserted into the catholyte flow plate and measured using a Bio-Logic VMP-3 or SP-200 potentiostat. The working electrode was prepared by dispersing 11 mg of $PdSe_2$ powder

in 2.5 mL of isopropanol with 25 µL of Nafion solution (5 wt%, Sigma-Aldrich) and then airbrushing this $PdSe_2$ catalyst dispersion onto a carbon fiber paper GDE with a microporous layer. The cathode was mounted onto a Teflon flow field and contacted using gold mesh or copper foil and the area of the cathode exposed to electrolyte was 5.7 cm^2. The anolyte flow plate chamber, separated by a Nafion-117 membrane, contained a plasma-treated carbon fiber paper electrode coated with ~25 mg cm^{-2} of platinized carbon (20 wt% Pt) for shorter term testing (Figure 4) and a GDE coated with ~2 mg cm^{-2} IrO_2 (>99.99%, <20 nm particle size, Fuel Cell Store) was used for longer term testing (Figure S20b). Neutral buffered electrolyte (0.25 M Na_2HPO_4/0.25 M $NaHPO_4$ = 0.5 M NaPi, pH ~6.5) was continuously cycled through both the cathode and anode chamber at a flow rate of 100 mL/h using a peristaltic pump. The O_2 flow rate was fixed at 100 sccm using a mass flow controller. 10 mL of buffered electrolyte was used in the cathode chamber. Aliquots of electrolyte solution were continuously taken during the electrolysis process by sampling through a septum inserted in the flow path, and then added to solutions of ~0.4 mM $Ce(SO_4)_2$ in 0.5 M H_2SO_4. The resulting change in absorbance of the solutions at 318 nm were then measured shortly thereafter by UV-Vis on a JASCO V-570 UV/Vis/NIR spectrophotometer. The observed absorbance values were converted to the corresponding concentration of H_2O_2 via the following equations:

$$2\,Ce^{4+} + H_2O_2 \rightarrow 2Ce^{3+} + O_2 + 2H^+$$

$$[H_2O_2]\,(in\ mM) = \frac{V_{Ce} * [Ce^{4+}]_{ref} - (V_{Ce} + V_{aliquot})[Ce^{4+}]_t}{2 * V_{aliquot}}$$

Where V_{Ce} is the volume of the $Ce(SO_4)_2$ solution that the aliquot is dropped into, $V_{aliquot}$ is the volume of the aliquot, $[Ce^{4+}]_{ref}$ is the concentration of the original $Ce(SO_4)_2$ reference solution,

and $[Ce^{4+}]_t$ is the concentration of the $Ce(SO_4)_2$ measured for a given timepoint. Subsequently, the Faradaic Efficiency for H_2O_2 production was calculated by the following equation:

$$Cumulative\ Faradaic\ Efficiency = \frac{Q_{H_2O_2}}{Q_{tot}} = \frac{2 * F * [H_2O_2] * V_{tot}}{Q_{tot} * 10^6}$$

Where F corresponds to Faraday's constant (in C/mol e^-), $[H_2O_2]$ is the H_2O_2 concentration (in mM) calculated from the previous equation, V_{tot} corresponds the total solution volume (in mL), and Q_{tot} is the total charge passed through the measurement (in C). The cumulative H_2O_2 selectivity can be calculated:

$$Cumulative\ H_2O_2\ Selectivity = \frac{200}{1 + \left(\frac{100}{Cumulative\ Faradaic\ Efficiency}\right)}$$

ICP-OES measurements. After the flow cell measurements, 5% HNO_3 was added to the remaining electrolyte in the cathode chamber to reach a total volume of 15 mL. Standards of $PdSO_4$ and SeO_2 were prepared in a mixture of 0.5 M NaPi buffer and 5% HNO_3 in a similar volume ratio. For digestion of $PdSe_2$, $PdSe_2$/GDE samples were immersed in 5% HNO_3 and sealed inside a stainless steel autoclave and heated at 120 °C for 12 hours. The Pd concentrations were determined using the average of the Pd 229.651 nm, 340.458 nm, and 360.955 nm atomic emission lines for Pd (with three replicates measured for each sample) and the Se concentrations using average of the 196.026 nm and 203.985 nm atomic emission lines for Se (with three replicates for each sample).

In-situ X-ray absorption spectroscopy measurements. In-situ XAS measurements were collected using a custom-built fluorescence detection H-cell (Figure S21) where the working electrode was mounted on the front using an acrylic or aluminum face plate, with the catalyst side facing inward to the electrolyte and the bare side facing back toward the incident X-rays and the

fluorescence detector. To contact the working electrode under the faceplate, a small piece of copper foil was used. A leakless Ag/AgCl reference electrode (Innovative Instruments Inc.) was secured in the front chamber with the working electrode and a graphite rod was used as the counter electrode in the back chamber, which was separated from the front chamber by a Nafion-117 membrane to minimize H_2O_2 crossover and decomposition. 2.5 mL of 0.5 M NaPi electrolyte was added to the front chamber for each measurement, and was kept under a continuous stream of O_2 gas throughout the duration of the measurement via a port in the top of the cell. The anode chamber was filled with the same electrolyte. XAS spectra were continuously collected during the electrolysis processes under various electrochemical potentials, with each displayed spectrum representing the average of at least three raw spectra collected under the same conditions.

ASSOCIATED CONTENT

Supporting Information Available: Additional figures and tables on the details of the DFT calculations, structural, spectroscopic and electrochemical characterizations of $PdSe_2$, Pd_4Se and $Pd_{17}Se_{15}$ catalysts (including post-electrocatalysis), long-term operational stability test of $PdSe_2$/GDE in a flow electrolyzer, elemental analysis of the digested catalysts and post-electrolysis electrolytes, in situ stability studies of $PdSe_2$ using synchrotron X-ray spectroscopies, and performance and stability comparison of various $2e^-$ ORR catalysts.

Corresponding Authors

***J.R. Schmidt** - Department of Chemistry, University of Wisconsin − Madison, 1101 University Avenue, Madison, Wisconsin 53706, United States; https://orcid.org/0000-0002-1438-117X; Email: schmidt@chem.wisc.edu

***Song Jin** - Department of Chemistry, University of Wisconsin − Madison, 1101 University Avenue, Madison, Wisconsin 53706, United States; http://orcid.org/0000-0001-8693-7010; Email: jin@chem.wisc.edu

ACKNOWLEDGEMENTS

This work is supported by the National Science Foundation (NSF) Grant CHE-1955074. Writing of the manuscript by R.D.R. was partially performed under the auspices of the U.S. Department of Energy by Lawrence Livermore National Laboratory (LLNL) under Contract DE-AC52-07NA27344. This research used resources of the Advanced Photon Source (APS), a U.S. Department of Energy (DOE) Office of Science User Facility operated for the DOE Office of Science by Argonne National Laboratory under contract no. DE-AC02-06CH11357. The authors thank Dr. George Sterbinsky, Dr. Joshua Wright and Dr. Mark Wolfman for assistance with XAS data collection at beamlines 9-BM, 10-ID, and 20-BM of the Advanced Photon Source, respectively. This work used facilities and instrumentation at the UW-Madison Wisconsin Centers for Nanoscale Technology (wcnt.wisc.edu) partially supported by the NSF through the Materials Research Science and Engineering Center (DMR-2309000), as well as at the UW-Madison Water Science and Engineering Laboratory (WSEL). We thank Steve Myers of the UW-Madison Chemistry machine shop for assistance in designing and fabricating the flow cell for H_2O_2 electrosynthesis and Dr. Rob McClain for use of the UV-Vis. We thank Willa Mihalyi-Koch, Dr. Chris R. Roy and Dr. Matthew T. Mayer for helpful discussions and additional sample characterizations.

COMPETING INTERESTS

A provisional patent has been filed based on this work by some of the authors of this manuscript (R.D.R., K.L., H.S., J.R.S., S.J.).

REFERENCES

(1) Yang, S.; Verdaguer-Casadevall, A.; Arnarson, L.; Silvioli, L.; Čolić, V.; Frydendal, R.; Rossmeisl, J.; Chorkendorff, I.; Stephens, I. E. L. Toward the Decentralized Electrochemical Production of H_2O_2: A Focus on the Catalysis. *ACS Catal.* **2018**, *8*, 4064–4081. https://doi.org/10.1021/acscatal.8b00217.

(2) Perry, S. C.; Pangotra, D.; Vieira, L.; Csepei, L.-I.; Sieber, V.; Wang, L.; Ponce de León, C.; Walsh, F. C. Electrochemical Synthesis of Hydrogen Peroxide from Water and Oxygen. *Nat Rev Chem* **2019**, *3*, 442–458. https://doi.org/10.1038/s41570-019-0110-6.

(3) Brillas, E.; Garcia-Segura, S. Benchmarking Recent Advances and Innovative Technology Approaches of Fenton, Photo-Fenton, Electro-Fenton, and Related Processes: A Review on the Relevance of Phenol as Model Molecule. *Sep. Purif. Technol.* **2020**, *237*, 116337. https://doi.org/10.1016/j.seppur.2019.116337.

(4) Sheng, H.; Janes, A. N.; Ross, R. D.; Hofstetter, H.; Lee, K.; Schmidt, J. R.; Jin, S. Linear Paired Electrochemical Valorization of Glycerol Enabled by the Electro-Fenton Process Using a Stable $NiSe_2$ Cathode. *Nat. Catal.* **2022**, *5*, 716–725. https://doi.org/10.1038/s41929-022-00826-y.

(5) Zhang, X.; Zhao, X.; Zhu, P.; Adler, Z.; Wu, Z.-Y.; Liu, Y.; Wang, H. Electrochemical Oxygen Reduction to Hydrogen Peroxide at Practical Rates in Strong Acidic Media. *Nat. Commun.* **2022**, *13*, 2880. https://doi.org/10.1038/s41467-022-30337-0.

(6) Gao, J.; Yang, H. bin; Huang, X.; Hung, S.-F.; Cai, W.; Jia, C.; Miao, S.; Chen, H. M.; Yang, X.; Huang, Y.; Zhang, T.; Liu, B. Enabling Direct H_2O_2 Production in Acidic Media through Rational Design of Transition Metal Single Atom Catalyst. *Chem* **2020**, *6*, 658–674. https://doi.org/10.1016/j.chempr.2019.12.008.

(7) Sheng, H.; Ross, R. D.; Schmidt, J. R.; Jin, S. Metal-Compound-Based Electrocatalysts for Hydrogen Peroxide Electrosynthesis and the Electro-Fenton Process. *ACS Energy Lett.* **2023**, *8*, 196–212. https://doi.org/10.1021/acsenergylett.2c01945.

(8) Jung, E.; Shin, H.; Lee, B.-H.; Efremov, V.; Lee, S.; Lee, H. S.; Kim, J.; Hooch Antink, W.; Park, S.; Lee, K.-S.; Cho, S.-P.; Yoo, J. S.; Sung, Y.-E.; Hyeon, T. Atomic-Level Tuning of Co–N–C Catalyst for High-Performance Electrochemical H_2O_2 Production. *Nat. Mater.* **2020**, *19*, 436–442. https://doi.org/10.1038/s41563-019-0571-5.

(9) Zhang, X.; Su, X.; Zheng, Y.; Hu, S.; Shi, L.; Gao, F.; Yang, P.; Niu, Z.; Wu, Z.; Qin, S.; Wu, R.; Duan, Y.; Gu, C.; Zheng, X.; Zhu, J.; Gao, M. Strongly Coupled Cobalt Diselenide Monolayers for Selective Electrocatalytic Oxygen Reduction to H_2O_2 under Acidic Conditions. *Angew. Chem. Int. Ed.* **2021**, *60*, 26922–26931. https://doi.org/10.1002/anie.202111075.

(10) Zheng, Y.; Hu, S.; Zhang, X.; Ju, H.; Wang, Z.; Tan, P.; Wu, R.; Gao, F.; Zhuang, T.; Zheng, X.; Zhu, J.; Gao, M.; Yu, S. Black Phosphorous Mediates Surface Charge Redistribution of CoSe 2 for Electrochemical H_2O_2 Production in Acidic Electrolytes. *Adv. Mater.* **2022**, *2205414*, 2205414. https://doi.org/10.1002/adma.202205414.

(11) Yan, M.; Wei, Z.; Gong, Z.; Johannessen, B.; Ye, G.; He, G.; Liu, J.; Zhao, S.; Cui, C.; Fei, H. Sb_2S_3-Templated Synthesis of Sulfur-Doped Sb-N-C with Hierarchical Architecture and High Metal Loading for H_2O_2 Electrosynthesis. *Nat. Commun.* **2023**, *14*, 368. https://doi.org/10.1038/s41467-023-36078-y.

(12) Jung, E.; Shin, H.; Hooch Antink, W.; Sung, Y.-E.; Hyeon, T. Recent Advances in Electrochemical Oxygen Reduction to H_2O_2 : Catalyst and Cell Design. *ACS Energy Lett.* **2020**, *5*, 1881–1892. https://doi.org/10.1021/acsenergylett.0c00812.
(13) Li, H.; Wen, P.; Itanze, D. S.; Hood, Z. D.; Adhikari, S.; Lu, C.; Ma, X.; Dun, C.; Jiang, L.; Carroll, D. L.; Qiu, Y.; Geyer, S. M. Scalable Neutral H_2O_2 Electrosynthesis by Platinum Diphosphide Nanocrystals by Regulating Oxygen Reduction Reaction Pathways. *Nat. Commun.* **2020**, *11*, 3928. https://doi.org/10.1038/s41467-020-17584-9.
(14) Dong, K.; Liang, J.; Wang, Y.; Zhang, L.; Xu, Z.; Sun, S.; Luo, Y.; Li, T.; Liu, Q.; Li, N.; Tang, B.; Alshehri, A. A.; Li, Q.; Ma, D.; Sun, X. Conductive Two-Dimensional Magnesium Metal−Organic Frameworks for High-Efficiency O_2 Electroreduction to H_2O_2. *ACS Catal.* **2022**, *12*, 6092–6099. https://doi.org/10.1021/acscatal.2c00819.
(15) Ross, R. D.; Sheng, H.; Ding, Y.; Janes, A. N.; Feng, D.; Schmidt, J. R.; Segre, C. U.; Jin, S. Operando Elucidation of Electrocatalytic and Redox Mechanisms on a 2D Metal Organic Framework Catalyst for Efficient Electrosynthesis of Hydrogen Peroxide in Neutral Media. *J. Am. Chem. Soc.* **2022**, *144*, 15845–15854. https://doi.org/10.1021/jacs.2c06810.
(16) Jiang, K.; Back, S.; Akey, A. J.; Xia, C.; Hu, Y.; Liang, W.; Schaak, D.; Stavitski, E.; Nørskov, J. K.; Siahrostami, S.; Wang, H. Highly Selective Oxygen Reduction to Hydrogen Peroxide on Transition Metal Single Atom Coordination. *Nat. Commun.* **2019**, *10*, 3997. https://doi.org/10.1038/s41467-019-11992-2.
(17) Lee, B.-H.; Shin, H.; Rasouli, A. S.; Choubisa, H.; Ou, P.; Dorakhan, R.; Grigioni, I.; Lee, G.; Shirzadi, E.; Miao, R. K.; Wicks, J.; Park, S.; Lee, H. S.; Zhang, J.; Chen, Y.; Chen, Z.; Sinton, D.; Hyeon, T.; Sung, Y.; Sargent, E. H. Supramolecular Tuning of Supported Metal Phthalocyanine Catalysts for Hydrogen Peroxide Electrosynthesis. *Nat. Catal.* **2023**, *6*, 234–243. https://doi.org/10.1038/s41929-023-00924-5.
(18) Ross, R. D.; Sheng, H.; Parihar, A.; Huang, J.; Jin, S. Compositionally Tuned Trimetallic Thiospinel Catalysts for Enhanced Electrosynthesis of Hydrogen Peroxide and Built-In Hydroxyl Radical Generation. *ACS Catal.* **2021**, *11*, 12643–12650. https://doi.org/10.1021/acscatal.1c03349.
(19) Kim, H.; Lim, J.; Lee, S.; Kim, H. H.; Lee, C.; Lee, J.; Choi, W. Spontaneous Generation of H_2O_2 and Hydroxyl Radical through O_2 Reduction on Copper Phosphide under Ambient Aqueous Condition. *Environ. Sci. Technol.* **2019**, *53*, 2918–2925. https://doi.org/10.1021/acs.est.8b06353.
(20) Back, S.; Na, J.; Ulissi, Z. W. Efficient Discovery of Active, Selective, and Stable Catalysts for Electrochemical H_2O_2 Synthesis through Active Motif Screening. *ACS Catal.* **2021**, *11*, 2483–2491. https://doi.org/10.1021/acscatal.0c05494.
(21) Chang, Q.; Zhang, P.; Mostaghimi, A. H. B.; Zhao, X.; Denny, S. R.; Lee, J. H.; Gao, H.; Zhang, Y.; Xin, H. L.; Siahrostami, S.; Chen, J. G.; Chen, Z. Promoting H_2O_2 Production via 2-Electron Oxygen Reduction by Coordinating Partially Oxidized Pd with Defect Carbon. *Nat. Commun.* **2020**, *11*, 1–9. https://doi.org/10.1038/s41467-020-15843-3.
(22) Wang, Y. L.; Gurses, S.; Felvey, N.; Boubnov, A.; Mao, S. S.; Kronawitter, C. X. In Situ Deposition of Pd during Oxygen Reduction Yields Highly Selective and Active Electrocatalysts for Direct H_2O_2 Production. *ACS Catal.* **2019**, *9*, 8453–8463. https://doi.org/10.1021/acscatal.9b01758.
(23) Yu, Z.; Lv, S.; Yao, Q.; Fang, N.; Xu, Y.; Shao, Q.; Pao, C.; Lee, J.; Li, G.; Yang, L.; Huang, X. Low-Coordinated Pd Site within Amorphous Palladium Selenide for Active, Selective,

and Stable H_2O_2 Electrosynthesis. *Adv. Mater.* **2022**, *35,* 2208101. https://doi.org/10.1002/adma.202208101.
(24) Yu, Z.; Xu, S.; Feng, Y.; Yang, C.; Yao, Q.; Shao, Q.; Li, Y. F.; Huang, X. Phase-Controlled Synthesis of Pd-Se Nanocrystals for Phase-Dependent Oxygen Reduction Catalysis. *Nano Lett.* **2021**, *21*, 3805–3812. https://doi.org/10.1021/acs.nanolett.1c00147.
(25) Sheng, H.; Janes, A. N.; Ross, R. D.; Kaiman, D.; Huang, J.; Song, B.; Schmidt, J. R.; Jin, S.; Sheng, H.; Janes, A.N.; Ross, R.D.; Kaiman, D.; Huang, J.; Song, B.; Schmidt, J.R.; Jin, S. Stable and Selective Electrosynthesis of Hydrogen Peroxide and the Electro-Fenton Process on $CoSe_2$ Polymorph Catalysts. *Energy Environ. Sci.* **2020**, *13*, 4189–4203. https://doi.org/10.1039/d0ee01925a.
(26) Gu, Y.; Zhang, L.; Cai, H.; Liang, L.; Liu, C.; Hoffman, A.; Yu, Y.; Houston, A.; Puretzky, A. A.; Duscher, G.; Rack, P. D.; Rouleau, C. M.; Meng, X.; Yoon, M.; Geohegan, D. B.; Xiao, K. Stabilized Synthesis of 2D Verbeekite: Monoclinic $PdSe_2$ Crystals with High Mobility and In-Plane Optical and Electrical Anisotropy. *ACS Nano* **2022**, *16*, 13900-13910. https://doi.org/10.1021/acsnano.2c02711.
(27) Irvine, C. T.; Hoefer, N.; Moser, M. J.; Nelson, R. A.; McComb, D. W.; Goldberger, J. E. Diselenide Dianion's Dual Powers: $PdSe_2$ Polymorph Control and Pd_3Se_{10} Superatomic Crystal Creation. *Chem. Mater.* **2023**, *35*, 4404–4411. https://doi.org/10.1021/acs.chemmater.3c00568.
(28) Chow, W. L.; Yu, P.; Liu, F.; Hong, J.; Wang, X.; Zeng, Q.; Hsu, C.-H.; Zhu, C.; Zhou, J.; Wang, X.; Xia, J.; Yan, J.; Chen, Y.; Wu, D.; Yu, T.; Shen, Z.; Lin, H.; Jin, C.; Tay, B. K.; Liu, Z. High Mobility 2D Palladium Diselenide Field-Effect Transistors with Tunable Ambipolar Characteristics. *Adv. Mater.* **2017**, *29*, 1602969. https://doi.org/10.1002/adma.201602969.
(29) Lu, L. S.; Chen, G. H.; Cheng, H. Y.; Chuu, C. P.; Lu, K. C.; Chen, C. H.; Lu, M. Y.; Chuang, T. H.; Wei, D. H.; Chueh, W. C.; Jian, W. B.; Li, M. Y.; Chang, Y. M.; Li, L. J.; Chang, W. H. Layer-Dependent and In-Plane Anisotropic Properties of Low-Temperature Synthesized Few-Layer $PdSe_2$ Single Crystals. *ACS Nano* **2020**, *14*, 4963–4972. https://doi.org/10.1021/acsnano.0c01139.
(30) Oyedele, A. D.; Yang, S.; Liang, L.; Puretzky, A. A.; Wang, K.; Zhang, J.; Yu, P.; Pudasaini, P. R.; Ghosh, A. W.; Liu, Z.; Rouleau, C. M.; Sumpter, B. G.; Chisholm, M. F.; Zhou, W.; Rack, P. D.; Geohegan, D. B.; Xiao, K. $PdSe_2$: Pentagonal Two-Dimensional Layers with High Air Stability for Electronics. *J. Am. Chem. Soc.* **2017**, *139*, 14090–14097. https://doi.org/10.1021/jacs.7b04865.
(31) Gu, Y.; Cai, H.; Dong, J.; Yu, Y.; Hoffman, A. N.; Liu, C.; Oyedele, A. D.; Lin, Y. C.; Ge, Z.; Puretzky, A. A.; Duscher, G.; Chisholm, M. F.; Rack, P. D.; Rouleau, C. M.; Gai, Z.; Meng, X.; Ding, F.; Geohegan, D. B.; Xiao, K. Two-Dimensional Palladium Diselenide with Strong In-Plane Optical Anisotropy and High Mobility Grown by Chemical Vapor Deposition. *Adv. Mater.* **2020**, *32,* 1906238. https://doi.org/10.1002/adma.201906238.
(32) Liang, Q.; Chen, Z.; Zhang, Q.; Wee, A. T. S. Pentagonal 2D Transition Metal Dichalcogenides: $PdSe_2$ and Beyond. *Adv. Funct. Mater.* **2022**, *32,* 2203555. https://doi.org/10.1002/adfm.202203555.
(33) Yu, J.; Kuang, X.; Li, J.; Zhong, J.; Zeng, C.; Cao, L.; Liu, Z.; Zeng, Z.; Luo, Z.; He, T.; Pan, A.; Liu, Y. Giant Nonlinear Optical Activity in Two-Dimensional Palladium Diselenide. *Nat. Commun.* **2021**, *12*, 1083. https://doi.org/10.1038/s41467-021-21267-4.

(34) Sheng, H.; Hermes, E. D.; Yang, X.; Ying, D.; Janes, A. N.; Li, W.; Schmidt, J. R.; Jin, S. Electrocatalytic Production of H_2O_2 by Selective Oxygen Reduction Using Earth-Abundant Cobalt Pyrite (CoS_2). *ACS Catal.* **2019**, *9*, 8433–8442. https://doi.org/10.1021/acscatal.9b02546.
(35) Mariano, R. G.; Wahab, O. J.; Rabinowitz, J. A.; Oppenheim, J.; Chen, T.; Unwin, P. R.; Dincă, M. Thousand-Fold Increase in O_2 Electroreduction Rates with Conductive MOFs. *ACS Cent. Sci.* **2022**, *8*, 975–982. https://doi.org/10.1021/acscentsci.2c00509.
(36) Sun, Y.; Silvioli, L.; Sahraie, N. R.; Ju, W.; Li, J.; Zitolo, A.; Li, S.; Bagger, A.; Arnarson, L.; Wang, X.; Moeller, T.; Bernsmeier, D.; Rossmeisl, J.; Jaouen, F.; Strasser, P. Activity–Selectivity Trends in the Electrochemical Production of Hydrogen Peroxide over Single-Site Metal–Nitrogen–Carbon Catalysts. *J. Am. Chem. Soc.* **2019**, *141*, 12372–12381. https://doi.org/10.1021/jacs.9b05576.
(37) Dong, K.; Xu, Z.; He, X.; Zhao, D.; Chen, H.; Liang, J.; Luo, Y.; Sun, S.; Zheng, D.; Liu, Q.; Alshehri, A. A.; Feng, Z.; Wang, Y.; Sun, X. Ultrathin Single-Crystal $PtSe_2$ Nanosheets for High-Efficiency O_2 Electroreduction to H_2O_2. *Chem. Commun.* **2022**, 10683–10686. https://doi.org/10.1039/d2cc04503f.
(38) Zhang, X.-L.; Su, X.; Zheng, Y.; Hu, S.-J.; Shi, L.; Gao, F.; Yang, P.-P.; Niu, Z.-Z.; Wu, Z.; Qin, S.; Wu, R.; Duan, Y.; Gu, C.; Zheng, X.-S.; Zhu, J.-F.; Gao, M. Strongly Coupled Cobalt Diselenide Monolayers for Selective Electrocatalytic Oxygen Reduction to H_2O_2 under Acidic Conditions. *Angew. Chem. Int. Ed.* **2021**, *60*, 26922–26931. https://doi.org/10.1002/anie.202111075.
(39) Zhao, X.; Wang, Y.; Da, Y.; Wang, X.; Wang, T.; Xu, M.; He, X.; Zhou, W.; Li, Y.; Coleman, J. N.; Li, Y. Selective Electrochemical Production of Hydrogen Peroxide at Zigzag Edges of Exfoliated Molybdenum Telluride Nanoflakes. *Natl. Sci. Rev.* **2020**, *7*, 1360–1366. https://doi.org/10.1093/nsr/nwaa084.
(40) Nørskov, J. K.; Rossmeisl, J.; Logadottir, A.; Lindqvist, L.; Kitchin, J. R.; Bligaard, T.; Jónsson, H. Origin of the Overpotential for Oxygen Reduction at a Fuel-Cell Cathode. *J. Phys. Chem. B* **2004**, *108*, 17886–17892. https://doi.org/10.1021/jp047349j.
(41) Koh, S. W.; Hu, J.; Hwang, J.; Yu, P.; Sun, Z.; Liu, Q.; Hong, W.; Ge, J.; Fei, J.; Han, B.; Liu, Z.; Li, H. Two-Dimensional Palladium Diselenide for the Oxygen Reduction Reaction. *Mater. Chem. Front.* **2021**, *5*, 4970–4980. https://doi.org/10.1039/d0qm01113d.
(42) Geiger, S.; Kasian, O.; Ledendecker, M.; Pizzutilo, E.; Mingers, A. M.; Fu, W. T.; Diaz-Morales, O.; Li, Z.; Oellers, T.; Fruchter, L.; Ludwig, A.; Mayrhofer, K. J. J.; Koper, M. T. M.; Cherevko, S. The Stability Number as a Metric for Electrocatalyst Stability Benchmarking. *Nat. Catal.* **2018**, *1*, 508–515. https://doi.org/10.1038/s41929-018-0085-6.
(43) Oyedele, A. D.; Yang, S.; Feng, T.; Haglund, A. V.; Gu, Y.; Puretzky, A. A.; Briggs, D.; Rouleau, C. M.; Chisholm, M. F.; Unocic, R. R.; Mandrus, D.; Meyer, H. M.; Pantelides, S. T.; Geohegan, D. B.; Xiao, K. Defect-Mediated Phase Transformation in Anisotropic Two-Dimensional $PdSe_2$ Crystals for Seamless Electrical Contacts. *J. Am. Chem. Soc.* **2019**, *141*, 8928–8936. https://doi.org/10.1021/jacs.9b02593.
(44) Liang, Q.; Zhang, Q.; Gou, J.; Song, T.; Arramel; Chen, H.; Yang, M.; Lim, S. X.; Wang, Q.; Zhu, R.; Yakovlev, N.; Tan, S. C.; Zhang, W.; Novoselov, K. S.; Wee, A. T. S. Performance Improvement by Ozone Treatment of 2D $PdSe_2$. *ACS Nano* **2020**, *14*, 5668–5677. https://doi.org/10.1021/acsnano.0c00180.
(45) Kresse, G.; Hafner, J. Ab Initio Molecular Dynamics for Liquid Metals. *Phys. Rev. B* **1993**, *47*, 558–561. https://doi.org/10.1103/PhysRevB.47.558.

(46) Kresse, G.; Furthmüller, J. Efficiency of Ab-Initio Total Energy Calculations for Metals and Semiconductors Using a Plane-Wave Basis Set. *Comput. Mater. Sci.* **1996**, *6*, 15–50. https://doi.org/10.1016/0927-0256(96)00008-0.
(47) Kresse, G.; Furthmüller, J. Efficient Iterative Schemes for Ab Initio Total-Energy Calculations Using a Plane-Wave Basis Set. *Phys. Rev. B* **1996**, *54*, 11169–11186. https://doi.org/10.1103/PhysRevB.54.11169.
(48) Larsen, A. H. The Atomic Simulation Environment - A Python Library for Working with Atoms. *J. Phys. Condens. Matter* **2012**, *29*, 273002.
(49) Kresse, G.; Joubert, D. From Ultrasoft Pseudopotentials to the Projector Augmented-Wave Method. *Phys. Rev. B - Condens. Matter Mater. Phys.* **1999**, *59*, 1758–1775. https://doi.org/10.1103/PhysRevB.59.1758.
(50) Perdew, J. P.; Burke, K.; Ernzerhof, M. Generalized Gradient Approximation Made Simple. *Phys. Rev. Lett.* **1996**, *77*, 3865. https://doi.org/10.1103/PhysRevLett.77.3865.
(51) Tkatchenko, A.; Scheffler, M. Accurate Molecular van Der Waals Interactions from Ground-State Electron Density and Free-Atom Reference Data. *Phys. Rev. Lett.* **2009**, *102*, 6–9. https://doi.org/10.1103/PhysRevLett.102.073005.
(52) Sun, M.; Chou, J. P.; Shi, L.; Gao, J.; Hu, A.; Tang, W.; Zhang, G. Few-Layer $PdSe_2$ Sheets: Promising Thermoelectric Materials Driven by High Valley Convergence. *ACS Omega* **2018**, *3*, 5971–5979. https://doi.org/10.1021/acsomega.8b00485.
(53) Mathew, K.; Kolluru, V. S. C.; Mula, S.; Steinmann, S. N.; Hennig, R. G. Implicit Self-Consistent Electrolyte Model in Plane-Wave Density-Functional Theory. *J. Chem. Phys.* **2019**, *151,* 234101. https://doi.org/10.1063/1.5132354.
(54) Mathew, K.; Sundararaman, R.; Letchworth-Weaver, K.; Arias, T. A.; Hennig, R. G. Implicit Solvation Model for Density-Functional Study of Nanocrystal Surfaces and Reaction Pathways. *J. Chem. Phys.* **2014**, *140*, 084106. https://doi.org/10.1063/1.4865107.
(55) Steinmann, S. N.; Michel, C.; Schwiedernoch, R.; Sautet, P. Impacts of Electrode Potentials and Solvents on the Electroreduction of CO_2: A Comparison of Theoretical Approaches. *Phys. Chem. Chem. Phys.* **2015**, *17*, 13949–13963. https://doi.org/10.1039/c5cp00946d.
(56) Gauthier, J. A.; Ringe, S.; Dickens, C. F.; Garza, A. J.; Bell, A. T.; Head-Gordon, M.; Nørskov, J. K.; Chan, K. Challenges in Modeling Electrochemical Reaction Energetics with Polarizable Continuum Models. *ACS Catal.* **2019**, *9*, 920–931. https://doi.org/10.1021/acscatal.8b02793.
(57) Monkhorst, H. J.; Pack, J. D. Special Points for Brillonin-Zone Integrations. *Phys. Rev. B* **1976**, *13*, 5188–5192. https://doi.org/10.1039/c8ta11250a.
(58) Steinmann, S. N.; Sautet, P.; Michel, C. Solvation Free Energies for Periodic Surfaces: Comparison of Implicit and Explicit Solvation Models. *Phys. Chem. Chem. Phys.* **2016**, *18*, 31850–31861. https://doi.org/10.1039/c6cp04094b.
(59) M. J. Frisch, G. W. Trucks, H. B. Schlegel, G. E. Scuseria, M. A. Robb, J. R. Cheeseman, G. Scalmani, V. Barone, G. A. Petersson, H. Nakatsuji, X. Li, M. Caricato, A. V. Marenich, J. Bloino, B. G. Janesko, R. Gomperts, B. M. Gaussian 16, Revision C.01, 2016. Gaussian Inc.: Wallingford, CT 2016.
(60) Marenich, A. V.; Cramer, C. J.; Truhlar, D. G. Universal Solvation Model Based on Solute Electron Density and on a Continuum Model of the Solvent Defined by the Bulk Dielectric Constant and Atomic Surface Tensions. *J. Phys. Chem. B* **2009**, *113*, 6378–6396. https://doi.org/10.1021/jp810292n.

(61) Henkelman, G.; Jónsson, H. Improved Tangent Estimate in the Nudged Elastic Band Method for Finding Minimum Energy Paths and Saddle Points. *J. Chem. Phys.* **2000**, *113*, 9978–9985. https://doi.org/10.1063/1.1323224.
(62) Henkelman, G.; Jónsson, H. A Dimer Method for Finding Saddle Points on High Dimensional Potential Surfaces Using Only First Derivatives. *J. Chem. Phys.* **1999**, *111*, 7010–7022. https://doi.org/10.1063/1.480097.
(63) Van Den Bossche, M.; Skúlason, E.; Rose-Petruck, C.; Jónsson, H. Assessment of Constant-Potential Implicit Solvation Calculations of Electrochemical Energy Barriers for H_2 Evolution on Pt. *J. Phys. Chem. C* **2019**, *123*, 4116–4124. https://doi.org/10.1021/acs.jpcc.8b10046.
(64) Tang, M. T.; Liu, X.; Ji, Y.; Norskov, J. K.; Chan, K. Modeling Hydrogen Evolution Reaction Kinetics through Explicit Water-Metal Interfaces. *J. Phys. Chem. C* **2020**, *124*, 28083–28092. https://doi.org/10.1021/acs.jpcc.0c08310.
(65) Cao, H.; Zhang, Z.; Chen, J.-W.; Wang, Y.-G. Potential-Dependent Free Energy Relationship in Interpreting the Electrochemical Performance of CO_2 Reduction on Single Atom Catalysts. *ACS Catal.* **2022**, *12*, 6606–6617. https://doi.org/10.1021/acscatal.2c01470.

For Table of Contents Only

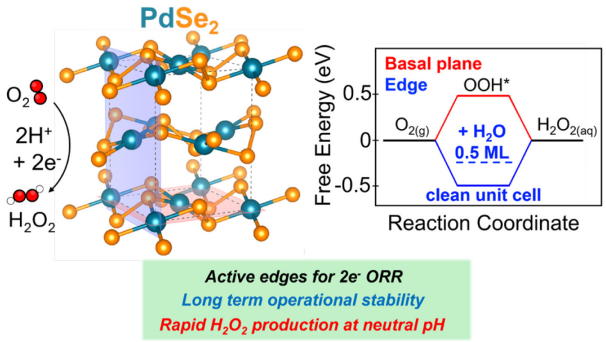

Active edges for 2e⁻ ORR

Long term operational stability

Rapid H_2O_2 production at neutral pH